ELSEVIER

Contents lists available at ScienceDirect

Remote Sensing of Environment

journal homepage: www.elsevier.com/locate/rse



Mapping three-dimensional variation in leaf mass per area with imaging spectroscopy and lidar in a temperate broadleaf forest



Adam Chlus*, Eric L. Kruger, Philip A. Townsend

Department of Forest and Wildlife Ecology, University of Wisconsin, Madison, WI, USA

ARTICLE INFO

Keywords: Leaf mass per area Lidar Imaging spectroscopy Three dimensional NEON AOP

ABSTRACT

Imaging spectroscopy is a valuable tool for mapping canopy foliar traits in forested ecosystems at landscape and larger scales. Most efforts to date have involved two-dimensional mapping of traits, typically representing top-of-canopy conditions. However, traits and their associated biological functions vary through the canopy vertical profile, such that incorporating information about vertical patterns may improve modeling of ecosystem processes like primary productivity. In 2016 and 2017, we collected extensive field data in forests in Domain 5 (Great Lakes) of the National Ecological Observatory Network (NEON) to characterize the vertical variation in leaf mass per area (LMA), an important foliar trait related to plant growth and defense. Fieldwork was coincident with NEON Airborne Observation Platform (AOP) overflights which collected imaging spectroscopy and lidar data. Using imaging spectroscopy to map top-of-canopy LMA and lidar to model vertical gradients of transmittance, we developed a method to map three-dimensional patterns in LMA in temperate broadleaf forests. Partial least squares regression (PLSR) was used to estimate top-of-canopy LMA (R^2 : 0.57, RMSE 10.8 g m $^{-2}$), which, along with lidar-derived metrics of light transmittance and height, was used in a multilevel regression to model within-canopy LMA (R^2 : 0.78, RMSE 8.3 g m $^{-2}$). The coupled models accurately estimated LMA throughout the canopy without taking into account species composition (R^2 = 0.82, RMSE: 8.5 g m $^{-2}$).

1. Introduction

The world's forest ecosystems are changing rapidly, and extensive data is necessary to better understand corresponding implications for ecosystem function and to accurately model future scenarios. However, traditional field-scale sampling techniques may not provide information at scales sufficient for characterizing landscape and broader-scale variation needed for accurate modeling. Remote sensing has long offered the potential to extrapolate sparse field measurements to generate inputs needed to drive models, especially of two-dimensional patterns across the land surface (Roughgarden et al., 1991; Cohen and Goward, 2004). However, forest ecosystems are inherently three-dimensional (3D) and multiple studies have highlighted the need to accurately characterize vertical patterns in structural and biophysical properties for parametrizing ecosystem process and forecasting models (Cavaleri et al., 2010; Coble et al., 2016; Rogers et al., 2017). For the most part, remote sensing products and ecosystem models ignore vertical variability in traits important to understanding forest processes.

A number of ecologically important structural, morphological and chemical properties vary throughout the vertical extent of forest canopies, including leaf area density (LAD), leaf angle distribution (LAD) and foliar chemical composition (e.g., concentrations of lignin and phosphorus, and δ^{13} C) (Vose et al., 1995; Niinemets et al., 2015; Leuning et al., 1991). Among the most widely studied and characterized biophysical properties in the context of within-canopy patterns is leaf mass per area (LMA), the ratio between the projected leaf area and dry mass, which is largely comprised of structural and nonstructural carbohydrates, proteins, lignin and minerals (Poorter et al., 2009). LMA—or its inverse, specific leaf area (SLA)—is a central component of the leaf economic spectrum (LES) representing the tradeoff between growth and defense (Wright et al., 2004; Poorter et al., 2009). For example, relatively thin leaves with low LMA tend to have high rates of photosynthesis per unit mass compared to denser, thicker and more durable leaves with high LMA (Niinemets, 1999; Wright et al., 2004). The drivers of LMA variation differ across scales. Broadly, LMA variation is largely driven by taxonomy, while local environment and site conditions can explain a large proportion of LMA variation at finer scales (Messier et al., 2010; Messier et al., 2017).

LMA decreases with depth into the canopy, owing primarily to the attenuation of light and a decrease in height-mediated hydraulic constraints (Cavaleri et al., 2010; Niinemets et al., 2015). Microclimatic variables including temperature, wind exposure and humidity, which

^{*} Corresponding author at: Department of Forest and Wildlife Ecology, University of Wisconsin-Madison, 1630 Linden Drive, Madison, WI 53706, USA. E-mail addresses: chlus@wisc.edu (A. Chlus), elkruger@wisc.edu (E.L. Kruger), ptownsend@wisc.edu (P.A. Townsend).

co-vary with incident radiation and height, also influence within-canopy LMA (Niinemets, 2001; Poorter et al., 2009; Petter et al., 2016; Wu et al., 2016). The degree to which within-canopy gradients in LMA are driven by irradiance or height is not universal and can vary as a function of species, local environmental conditions and seasonality (Koch et al., 2004; Coble and Cavaleri, 2014; Coble et al., 2016). While numerous studies have explored within-canopy patterns in LMA through individual tree canopies (Ellsworth and Reich, 1993; Aranda et al., 2004), few studies have explored patterns of LMA in vertically heterogenous canopies where both species composition and architecture vary within the vertical profile. The ability to understand these patterns in three dimensions may provide insights into spatial patterns of forest responses to change, ranging from successional responses to disturbances at local scales to landscape-level responses to broad-scale stresses such as drought or the cumulative impacts of climate change. As well, 3D profiles of canopy traits may also enable more accurate parameterization of landscape- and larger-scale process models that do not typically represent spatial variation of the vertical distribution of canopy traits.

Here we present a remote sensing approach that utilizes imaging spectroscopy and lidar to characterize the 3D variation in LMA in broadleaf canopies (Fig. 1). Our approach is based on the large body of research that has demonstrated that LMA decreases through the canopy from top to bottom and that decrease is largely driven by incident irradiance and/or height mediated hydraulics constraints (Ellsworth and Reich, 1993; Koch et al., 2004; Poorter et al., 2009). We posit that if we are able to estimate LMA at the top of the canopy and model the withincanopy environmental gradients that are known to drive top-down decreases in LMA, we should be able estimate within-canopy (topdown) patterns in LMA. Our method uses airborne imaging spectroscopy to estimate LMA at the top of the canopy and lidar to model within-canopy environmental gradients driving top down patterns in LMA. Imaging spectroscopy provides the most direct approach to foliar trait estimation at large scales, including LMA (Asner et al., 2015; Singh et al., 2015; Chadwick and Asner, 2016; Wang et al., 2019, 2020). While lidar provides the ability to penetrate the canopy and enables characterization of the 3D light environment (Lefsky et al., 2002; Todd et al., 2003; Olpenda et al., 2018). Our method builds on the work of Parker et al. (2001) who demonstrated that estimates of vertical light transmittance derived from lidar follow vertical patterns in photosynthetically active radiation (PAR) and Fleck et al. (2004) who found with-canopy LMA tracked with-canopy irradiance estimated using terrestrial lidar. We demonstrate this approach with airborne imaging spectroscopy and lidar data from the U.S. National Ecological Observatory Network (NEON) coupled with coincidence

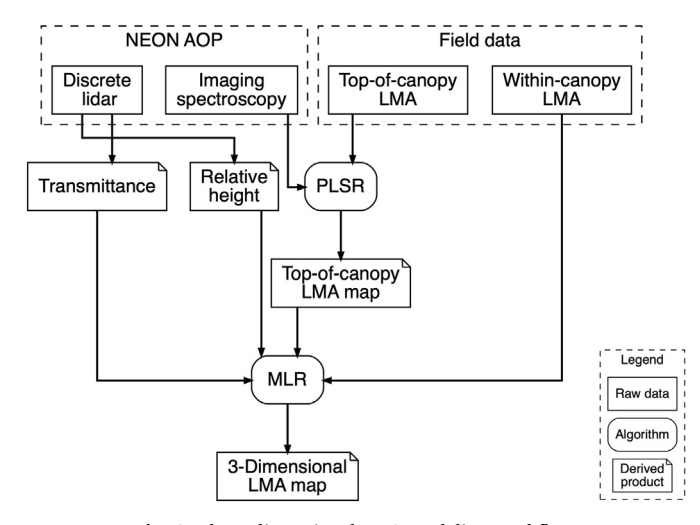


Fig. 1. Three-dimensional LMA modeling workflow.

measurements that we use to parameterize our model.

2. Methods

2.1. Study Area

Our study area consisted of hardwood-dominated forests in northern Wisconsin and Michigan's Upper Peninsula (89.5 W, 46.0 N). The area is characterized by a mix of managed and unmanaged stands of various age classes, species composition and structure. Common broadleaf deciduous species include trembling and bigtooth aspen (Populus tremuloides and P. grandidentata), sugar and red maple (Acer saccharum and A. rubrum), red oak (Ouercus rubra), black and white ash (Fraxinus nigra and F. americana), basswood (Tilia americana) and paper and yellow birch (Betula papyrifera and B. alleghaniensis). Fieldwork was conducted in sites within the Great Lakes ecoregion of the National Ecological Observatory Network. NEON is a continental scale network of long-term monitoring sites distributed across ecoregions within the United States. Each ecoregion contains multiple sites that are the focus of environmental monitoring activities including plant and animal surveys, soil characterization and airborne remote sensing data collection. Sampling took place within three NEON sites in the ecoregion: UNDE, CHEQ, and STEI (Fig. 2). Sites range in size from 40-200 km² and comprise a mix of private, municipal, state and federally-owned land

2.2. Remote sensing data

Remote sensing data were collected between September 2-12, 2016 and September 1-12, 2017 by NEON's Airborne Observatory Platform (AOP). AOP is a multi-sensor system which includes an imaging spectrometer, lidar sensor and a high resolution RGB camera. The imaging spectrometer is an AVIRIS-NG-like sensor built by NASA's Jet Propulsion Laboratory that measures radiation from 380-2510 nm in 420 bands, with a spectral sampling width of approximately 6 nm (Kampe et al., 2010; Kampe et al., 2011). Lidar data were collected using an Optech ALTM 3500 Gemini, which is a dual sensor instrument consisting of a full waveform digitizer and discrete return sensor transmitting at 1064 nm. The instrument was operated at a pulse frequency of 100 Hz and recorded up to four returns. The AOP system was flown on a DeHavilland DHC-6 Twin Otter at 1000 m above ground level (a.g.l.), resulting in 1 m resolution imaging spectroscopy data and a discrete return density of \sim 4 pts. m $^{-2}$. The full waveform lidar and RGB camera data were not used in this study.

Orthorectification of the imaging spectroscopy data and co-location with the lidar data was performed by NEON using a ray tracing algorithm coupled with measurements from an onboard inertial measurement unit (IMU) and GPS (Kampe et al., 2016). Surface reflectance was generated using ATCOR 4 (ReSe, Wil, Switzerland), which approximates atmospheric conditions including water vapor and aerosol content using the MODTRAN radiative transfer code (Richter and Schläpfer, 2015). The surface reflectance imagery exhibited strong cross-track gradients in brightness due to varying viewing and solar geometry. To remove the brightness gradients, we applied a semi-empirical bidirectional reflectance distribution function (BRDF) correction employing the widely used Ross-Li kernel combination to model the volumetric, geometric and isometric scattering components (Colgan et al., 2012; Schläpfer et al., 2014). A single set of BRDF correction coefficients was generated for each site and date by randomly sampling 10% of the pixels from each flightline and pooling the sampled data before fitting the BRDF correction model. Because scattering properties are dependent on surface type, we limited the BRDF correction model to vegetated pixels using an NDVI threshold of 0.6. Following the BRDF correction, all images were resampled to an interval of 5 nm (ex. 400 nm, 405 nm, ...) using a Gaussian approximation of the spectral response function. Resampling was performed to harmonize

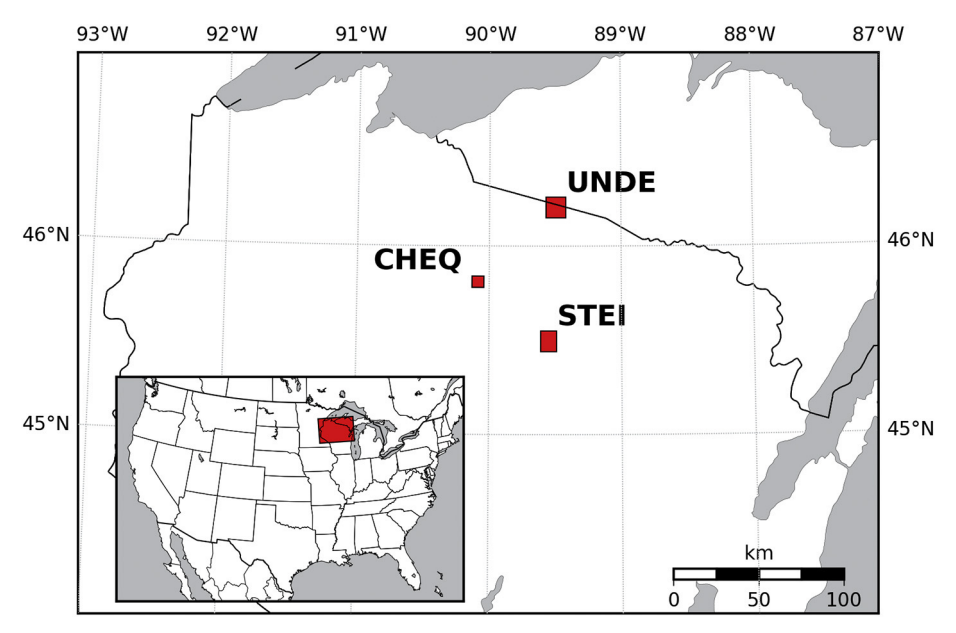


Fig. 2. Flight boxes and sampling boundaries for the three sites within the NEON Great Lakes ecoregion.

interannual images which had different wavelength centers due to annual radiometric calibrations. Before analyses, water absorption features (1330–1430 nm and 1800–1960 nm) and spectrum tails (< 400 nm and > 2450 nm) were removed from the imagery due to low signal to noise.

Discrete lidar data were normalized against a 1 m digital elevation model (DEM) to derive height above ground for each return. The DEM was created by NEON from the discrete return lidar data using a triangulated irregular network of ground returns interpolated to a surface (Goulden, 2019).

2.3. Field sampling

Field sampling occurred within 10 days of AOP overflights in 2016 and 2017 and involved plot-level collection of leaves throughout the vertical profile of the canopy. Plot locations were manually chosen to capture the range of forest types within the ecoregion and were distributed throughout the study area. Prior to sampling, a comprehensive survey of each plot was conducted. Species, diameter at breast height (DBH), crown class (dominant, codominant or suppressed) and location within the plot were recorded for all trees with DBH greater than 5 cm that had foliage within the plot. Trees were labeled dominant or codominant if their crowns were in the exposed upper canopy, that is they were visible from above, had sunlit foliage and were not completely obstructed by other trees, while all other trees were designated suppressed. Because GPS positions are known to have large errors under closed canopy conditions, all plots were revisited to survey the plot center coordinates during the fall of the sampling year once the trees had dropped their leaves (Sigrist et al., 1999). GPS measurements were made using a Geo7x with an external Zephyr 2 antenna (Trimble Inc., Sunnyvale, CA, USA) mounted on a 2 m range pole and were differentially corrected after collection to an accuracy of < 2 m.

Following the plot survey, branches were sampled throughout the vertical profile of the canopy, independent of species or individual tree. The number of branches within the canopy that were sampled depended on the number of species present in the plot and structural complexity of the canopy. Branches were sampled using a variety of tools depending their location in the canopy. Branches less than 15 m a.g.l. were collected using extendable pole pruners. Between 15 m and the top of the canopy, a Big Shot throw weight launcher (Sherrill Tree, Greensboro, NC, USA) was used to launch a line into the canopy, from

which a custom-built cutting device (à la Poulter et al., 1991) was raised to retrieve branches. For sun exposed branches (i.e., top-of-canopy) greater than 15 m, either a shotgun or a second custom cutter (Supplemental Fig. S1) was used to retrieve the top-of-canopy branch. Whenever possible, we attempted to sample every tree with foliage in the plot at multiple heights. In some plots, whether due to the number of trees within the plot or inaccessibility, not every tree was sampled.

The height (a.g.l.) of all branches, except those collected using a shotgun, were measured directly using a measuring tape that was attached to the cutting device. For branches sampled with a shotgun, the branch height was either measured using a laser hypsometer (Haglöf, Sweden), measuring tape, or, in a select few cases, was estimated from the lidar data. For each sampled branch, we calculated its relative height in the canopy, which was defined as the ratio between the field-measured branch height and maximum lidar return height within the plot.

The only differences in sampling between years were: 1) in 2016, 5-m diameter circular plots were used versus 5 \times 5 m square plots in 2017, and 2) 3 and 10 leaves per height were sampled in 2016 and 2017, respectively. Plot shape was changed between years to increase plot size and to simplify sampling. The number of leaves collected per height was increased to better capture within branch variability in LMA

After leaves were collected, reflectance measurements were made using a full-range (350-2500 nm) field spectrometer equipped with a leaf clip to estimate LMA using spectroscopic models. Leaf measurements were referenced against a measurement on a 99% white Spectralon panel (Labsphere, North Sutton, NH, USA) to derive relative reflectance. Measurements were typically taken immediately after collection; when that was not possible, leaves were placed in a plastic bag with a damp paper towel and stored in a cooler on ice until measurements could be made, within 2 h. Reflectance spectra were measured in 2016 with a Fieldspec 3 spectrometer (Analytical Spectral Devices, Boulder, CO, USA) and in 2017 with a PSR 3500+ spectrometer (Spectral Evolution, Boston, MA, USA). After reflectance measurements were complete, leaf samples were stored in a cooler until leaf area measurements were made later the same day. Leaf area was measured on three leaves per branch using a LI-3100 leaf area meter (LI-COR Biosciences, Lincoln, NE, USA), after which samples were frozen and stored for further analysis. Once the samples were returned to the lab. they were dried to constant mass in a freeze dryer (> 120 h) and weighed. Dry weights were divided by the projected fresh leaf area to calculate LMA.

LMA has shown to be robustly measurable from fresh leaf spectroscopy across a wide range of leaf types using spectrometers from multiple manufacturers (Serbin et al., 2019). As such, LMA was estimated for leaves that were not directly measured using spectroscopic models. Models were developed using partial least squares regression (PLSR), a common chemometric technique (Wold et al., 2001), in Python using the package 'scikit-learn' (Pedregosa et al., 2011). Spectroscopic models were built using linked reflectance and LMA measurements made during this study, and separate models were generated for each year to account for spectrometer-specific differences in reflectance measurements. Prior to model development, we removed spurious data points using a Bonferroni-corrected outlier detection test (Dupuis and Hamilton, 2000), less than 1% of data points were identified as outliers. Following outlier removal, the dataset was split randomly 50:50 into calibration and validation datasets. Using the calibration data, we then computed the optimal number of model components using the crossvalidated predicted residual sum of squares (PRESS) statistic using the adjusted Wold's R as a selection criterion (p = 0.05) (Li et al., 2002). The calibration dataset was used to build a series of 500 models, each model was built using a random 70% split of the calibration dataset. The 500 models were applied to the validation dataset and the mean predictions were compared to observed LMA values and model performance was assessed using the root mean squared error (RMSE), coefficient of determination (R2) and bias. Following the accuracy assessment, 500 new permuted models were built using the entire dataset and were applied to the spectra of unmeasured leaves to estimate leaflevel LMA. Branch-level LMA was calculated as the average leaf-level LMA of the 3 or 10 leaves from each branch.

2.4. Top-of-canopy LMA

Branch-level LMA was scaled to the canopy level by averaging LMA from all sunlit branches from each plot. Predictive models linking field-measured canopy-level LMA and imaging spectroscopy data were developed using the same modeling approach, PLSR, that was used for developing leaf-level spectroscopic models. Plot spectra were extracted from a 7×7 pixel window around each plot center, which was a slightly larger window than the field plot area, to account for GPS and image registration error. All pixels within the 7×7 window were averaged, not discriminating between sunlit and shaded pixels, resulting in a single spectrum per plot. This approach makes our method more transferable to spaceborne imagers with larger pixel sizes in which shaded and sunlit portions of tree crowns will be mixed in pixels. When a plot was covered by multiples lines owing to flightline overlap, we averaged pixels from all flightlines to produce a single reflectance spectrum.

A range of regions of the reflectance spectrum have been used to develop predictive models for LMA from spectroscopy data in the literature. At the leaf level, the full spectrum (Yang et al., 2016), spectral region subsets (Ourcival et al., 1999; Serbin et al., 2014) and variable selection techniques (Le Maire et al., 2008; Zhao et al., 2013) have been employed. At the canopy level, the full spectrum (400-2500 nm) is generally used (Singh et al., 2015; Chadwick and Asner, 2016; Wang et al., 2019). However Ali et al. (2016) found that the SWIR region from 1500-2500 nm exhibited the strongest correlation with canopy-level LMA, which is consistent with research showing that the shortwave infrared (SWIR) contains a number of absorption features related to dry matter content (Peterson et al., 1988; Curran, 1989; Jacquemoud et al., 1996). To assess the impact of spectral region selection on estimating top-of-canopy LMA, we compared the results of models built using four spectral regions moving to progressively longer wavelengths: 1) full spectrum (400-2450 nm), 2) NIR and SWIR (800-2450 nm), 3) the full SWIR (1600-2450 nm), and 4) far SWIR (2000-2450 nm).

Prior to model development, we performed a Bonferroni-corrected

outlier test and identified a single plot as a significant outlier, which was removed from further analysis. The optimal number of PLSR model components was selected by minimizing the cross-validated PRESS statistic using the adjusted Wold's R as a selection criterion (p = 0.05).

2.5. Transmittance

Lidar transmittance was calculated following the same form used by Parker et al. (2001) to model photosynthetically active radiation (PAR) transmittance from full-waveform lidar:

$$\tau(h) = 1 - \frac{N_{\geq h}}{N_{total}} \tag{1}$$

where τ is the lidar transmittance metric at height h above ground, $N_{\geq h}$ is the number of returns at or above height h and N_{total} is the total number of returns within the plot window. The fraction in Eq. (1) is equivalent to the interception/reflection rate of pulses above a given height. All returns were used when calculating transmittance metrics. Transmittance metrics were calculated at 1 m intervals throughout the canopy and were interpolated using a linear function to estimate transmittance at sampled branch heights in each plot.

Shallow lidar pulse penetration is a common issue in dense canopies where pulse energy may not reach the lower canopy, understory and ground (Fig. 3). A lack of returns from within the canopy can result in an underestimation of transmittance. We compared a range of window sizes from 5–100 m and found that, with increasing window size, model performance rapidly increased up until 20 m, after which the model performance stabilized, followed by a rapid decline with window sizes greater than 50 m (Supplemental Fig. S2). Based on these results we used a 20 m wide window around each plot to extract lidar returns for calculating transmittance.

2.6. Within-canopy LMA

Vertical gradients in LMA were modeled using multilevel linear regression (MLR). MLR was used to account for the hierarchical structure of the dataset in which variables could be divided into two levels: group (top-of-canopy LMA) and individual (transmittance and absolute and relative heights), where individual-level variables are nested within groups. MLR models present a compromise between complete and nopooling of data within groups and result in lower standard errors compared to traditional linear regression modeling (Gelman and Hill, 2007). In addition, MLR models can be formulated such that coefficients, intercepts and slopes are modeled as a function of group-level predictors. Models were fit in R using the package 'lmer' (Bates et al., 2015), group- and individual-level predictors were fit as fixed effects, and plot ID was treated as a random effect. We compared a range of models, beginning with univariate models and sequentially increasing model complexity by including additional individual-level predictors and a group-level predictor along with interaction terms. Note that we reverse the values of relative height and transmittance such that values range from 0 at the top of the canopy to 1 at ground level, this has benefits for fitting no-intercept regression models based on top-of-canopy LMA; that is, LMA predicted at a the top of the canopy where both relative height and transmittance are equal to zero will be simply the prediction of top-of-canopy LMA derived from imaging spectroscopy because any modifiers in our model based on these two metrics will be multiplied by zero.

2.7. Model evaluation

The performance of both top-of-canopy LMA and within-canopy LMA models were assessed using a 5 by 5-fold repeated cross-validation. Data splits were performed at the plot level to ensure that test and training datasets were independent. For each training-test split, the training data were first used to develop a PLSR model to predict top-of-

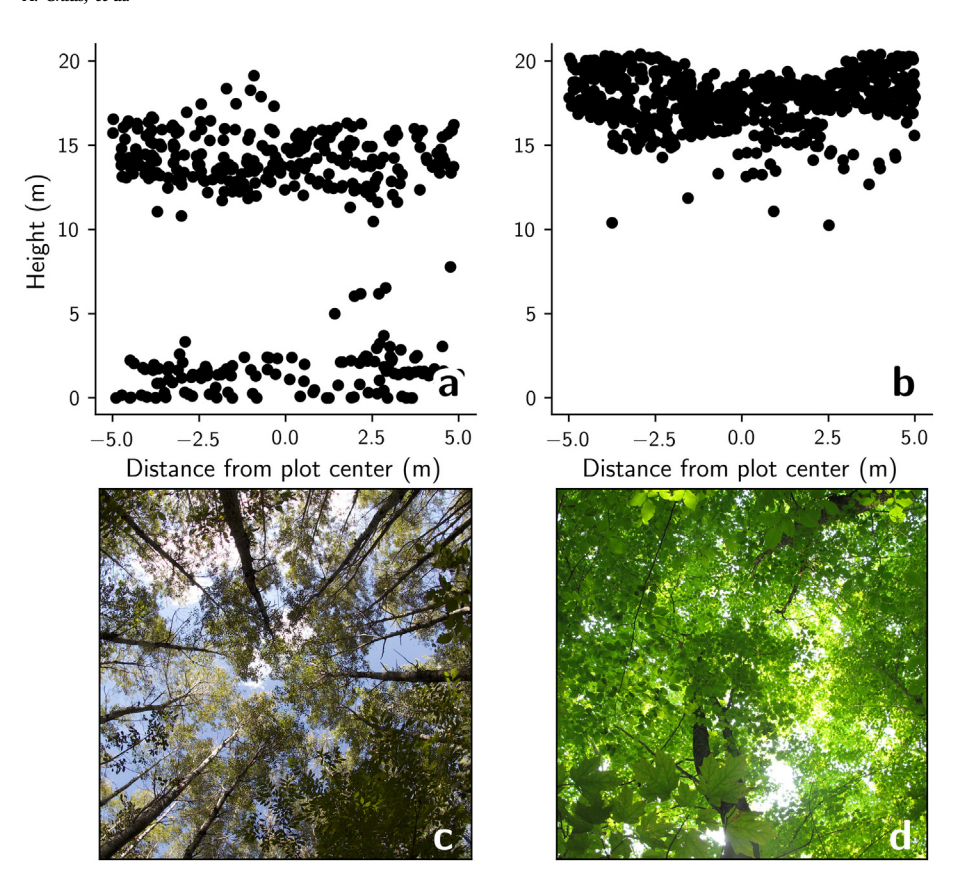


Fig. 3. Example of varying lidar penetration depth from two plots: a trembling aspen stand (a,c) and sugar maple stand (b,d); a–b) profile view of all returns; c–d) upward looking field photos from each plot. Both plots have a large number of returns from the upper canopy and few to no returns from the middle of the canopy. In the aspen stand the lack of returns from the middle canopy is consistent with branching structure seen in the field photos, while the lack of returns in the maple stand is the result of near complete beam attenuation in the upper canopy.

canopy LMA on the training dataset. These top-of-canopy LMA estimates were then used as inputs to the within-canopy MLR model along with the within-canopy training data. The derived top-of-canopy and within-canopy models were then applied to the test dataset in the same fashion, keeping the same test and training sets separate for each iteration. We report R², RMSE and %RMSE for both the training and test datasets.

2.8. Full-canopy LMA mapping

Following top-of-canopy and within-canopy model evaluation, we developed 3D maps of LMA across the entire study area using the best performing combination of models as determined by the out-of-sample performance metrics. The final model for implementation was generated using a permutation based approach whereby we generated 500 models each built using a random 70% of the data, we recorded the mean estimate predicted from the 500 models. Models were applied on 5×5 m horizontal pixel scale corresponding to the scale of field sampling and at 1 m intervals vertically. Downscaling of the imaging spectroscopy data utilized 5×5 pixel aggregation and averaging. Transmittance metrics were calculated at 1 m intervals using the 5 m pixel center for determining the neighborhood window center.

3. Results

Our dataset consisted of 59 plots, 18 sampled in 2016 and 41 in 2017. Fewer branches were sampled on average per plot in 2017 vs 2016 (12 vs 18 branches) to increase the number of plots sampled. A total of 14 broadleaf species were sampled during the study, 12 of which were present in the top of the canopy in at least one plot. Sugar maple (A. saccharum) was the most commonly sampled species accounting for 37% of the branches. Sugar maple is shade tolerant and is a ubiquitous understory species in the study area (Table 1). On average, 5.9 trees were sampled per plot and 84% of those had branches sampled

Table 1 Field sampling summary.

Species	Plots	Branches	Top-of- canopy branches	Mean branch LMA (g m ⁻²)	Range branch LMA (g m ⁻²)
Acer rubrum	10	33	2	52.6	33.0-86.1
Acer saccharum	39	301	22	40.5	23.2-94.9
Betula alleghaniensis	4	24	1	41.5	25.0-90.1
Betula papyrifera	7	30	4	51.5	29.7-102.6
Corylus cornuta	9	12	0	35.9	26.1-49.8
Fraxinus americana	8	24	7	61.2	20.2-102.8
Fraxinus nigra	7	51	7	51.8	26.2-100.4
Ostrya virginiana	8	17	0	28.5	23.5-36.3
Populus grandidentata	7	44	8	72	49.4-102.0
Populus tremuloides	13	64	21	74.1	52.9-102.1
Prunus spp.	6	13	2	56.4	36.6-88.6
Quercus rubra	18	144	21	71.7	32.2-120.7
Tilia americana	9	43	6	49.1	20.2-87.4
Ulmus americana	1	11	1	43.5	25.3–68.9

at multiple heights with the canopy.

Independent validation of leaf-level spectroscopic models exhibited high accuracies for estimating LMA from fresh spectra for both years of measurements (ASD 2016: $\rm R^2$: 0.98, RMSE: 2.9 g m $^{-2}$; PSR 2017: $\rm R^2$: 0.96, RMSE 4.5 g m $^{-2}$, Supplemental Figs. S3, S4). Branch-level LMA ranged from 20.2–120.7 g m $^{-2}$, while sampled branch heights ranged from 0.25–27.7 m a.g.l. (Fig. 4). The number of species in each plot varied from 1–7, with a mean of 2.5; multiple species were sampled in 44 of 59 plots.

3.1. Top-of-canopy LMA

Cross-validated results of PLSR models for top-of-canopy LMA from imaging spectroscopy data varied in performance depending on spectral

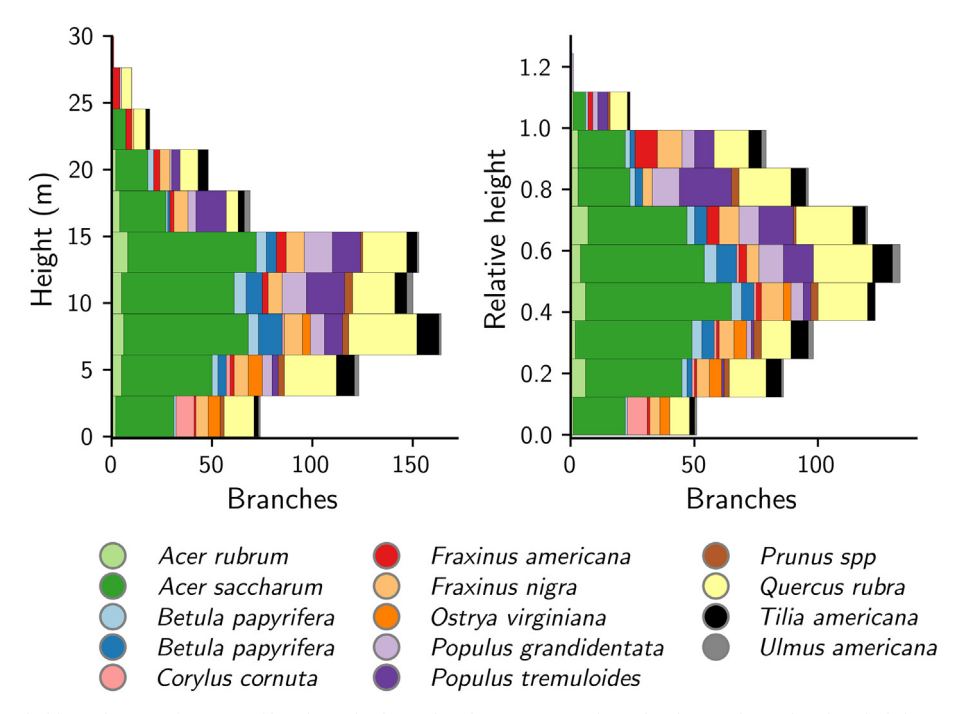


Fig. 4. Distribution of sampled branches as a function of height and relative height. Note: some branches have relative heights slightly greater than 1 as a result of an underestimation of maximum canopy height by the lidar sensor.

Table 2
Cross-validated PLSR top-of-canopy LMA results.

		Training		Test			
Wavelengths (nm)	Components	R ²	RMSE	%RMSE	R ²	RMSE	%RMSE
400–2450 800–2450 1600–2450 2000–2450	7 6 6	0.71 0.7 0.73 0.73	8.75 8.84 8.49 8.39	12.6 12.74 12.24 12.08	0.39 0.46 0.54 0.57	12.68 11.91 10.99 10.67	18.27 17.15 15.83 15.37

interval (Table 2). Model performance increased with narrower spectral ranges from full spectrum (400–2450 nm: $R^2\colon 0.39$, RMSE 12.7 g m $^{-2})$ to the far SWIR (2000–2450 nm: $R^2\colon 0.57$, RMSE 10.7 g m $^{-2})$ (Fig. 5). We used the top performing model, far SWIR, for the remainder of the analysis.

3.2. Within-canopy LMA

Within-canopy variables—height, relative height and lidar transmittance—all correlated positively with LMA (Fig. 6). Univariate models which considered only within-canopy variables ranged widely in predictive performances: transmittance (R²: 0.61, RMSE: $10.9~g~m^{-2}$) was the best performing, followed by relative height (R²: 0.43, RMSE $13.2~g~m^{-2}$) and height (R²: 0.14, RMSE $16.3~g~m^{-2}$).

Among the model forms tested, we found Eq. (2) exhibited the best results based on metrics of model performance, parsimony and interpretability (R²: 0.78, RMSE 8.3 g m⁻², Fig. 7), using a no-intercept model as described in 2.7 above. (See supplemental Table S1. for results of all tested models).

$$LMA(h) = LMA_{toc} + \tau_{inv_{20m}}(h) \cdot (\beta_0 + LMA_{toc} \cdot \beta_1 + rh_{inv}(h) \cdot \beta_2)$$
 (2)

where

 $h = height \ above \ ground \ (m)$

 $LMA_{toc} = Top \ of \ canopy \ LMA$

 $\tau_{inv_{20m}}$ = Inverted transmittance of window width 20 m at height h

 $rh_{inv} = Inverted relative height at height h$

Functionally, this model estimates LMA within a canopy as a function of top-of-canopy LMA, relative position in the canopy and transmittance. Regression coefficients modify the slope of transmittance as a function of relative height and top-of-canopy LMA.

Cross validation metrics varied across species (R²: 0.35–0.9; RMSE: 5.6–11.1 g m⁻²; Table 4). With the exception of *Ostrya virginiana*, which displayed little variation in LMA (23.5–36.3 g m⁻²), the within-canopy model was able to explain at least 50% of the variation in within-canopy LMA and at least 70% for 8 of the 14 species sampled. Normalized RMSE was less than or equal to 15% for all but 4 species (*O. virginiana*, *C. cornuta*, *P. tremuloides*, *Prunus spp.*). In an analysis of residuals, means for sugar maple, river birch, ironwood, red oak and bigtooth and trembling aspen showed small but significant differences from 0 (p < .01, Fig. 8a). The mean and median residuals for all species were within +/-7 g m⁻², which is lower than the RMSE of the top-of-canopy LMA model. Likewise, the residuals for canopy dominant trees differed from 0 (p < .01), but by less than 4 g m⁻² on average (Fig. 8b).

3.3. Three-dimensional LMA mapping

Three-dimensional maps of LMA were generated using the combination of the far SWIR PLSR model to estimate top-of-canopy LMA and Eq. (2). to estimate within-canopy LMA. Overall accuracy of the coupled model considering both top-of-canopy LMA and within-canopy LMA estimates was high ($R^2 = 0.82$; RMSE: $8.5 \, \mathrm{g \ m^{-2}}$).

We applied the model to entire study area and highlight a subset of the CHEQ site in three different visualizations of the 3D patterns in LMA: a horizontal map (Fig. 9a), a profile view across a transect (Fig. 9b) and vertical profiles for several forest types along the transect (Fig. 9d).

The horizontal map displays LMA at three heights: top-of-canopy, 5 m into the canopy and 10 m into the canopy, in the red, blue and green channels, respectively. Areas with relatively high LMA throughout the canopy are colored white, and include an open-grown

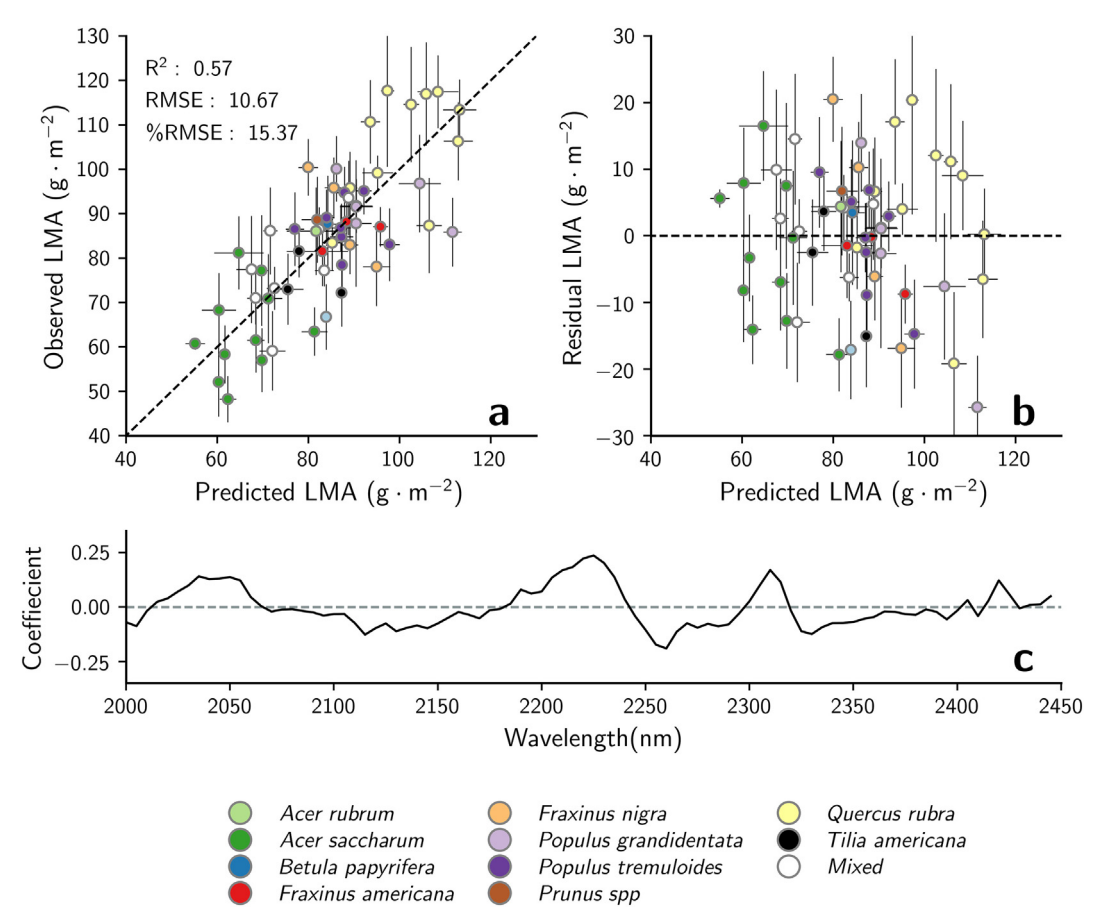


Fig. 5. Out-of-sample validation results for the top preforming top-of-canopy PLSR model using wavelengths 2000–2450 nm. a) Mean predicted versus observed; b) residuals; c) PLSR model coefficients; X-axis error bars on a and b indicate +/-1 standard deviation of out-sample LMA estimates across five cross-validation iterations; Y-axis error bars indicate +/-1 standard deviation of within-branch field measured LMA. Dot colors indicate top-of-canopy species composition.

oak stand (Oo) and aspen stand (Ta) annotated on the map. Purple regions, like the thinned oak stand (To), indicate relatively high LMA in the lower canopy, while the darkly colored maroon regions indicate relatively low LMA throughout the canopy and are generally representative of sugar maple stands (Sm).

4. Discussion

Here we demonstrate a novel method using imaging spectroscopy to estimate top-of-canopy LMA and lidar-derived metrics of within-canopy environmental gradients to map 3D profiles of within-canopy LMA. Our model works within northern temperate broadleaf forests and is independent of information on horizontal or vertical species composition. Prior studies have used imaging spectroscopy to map top-of-canopy LMA or scaled whole-canopy LMA, but this study is the first of its kind to map LMA at discrete intervals throughout the canopy.

The straightforward and computationally efficient lidar transmittance metric we used captured a large portion of the variation in withincanopy LMA. From a technical perspective, our comparison of transmittance window sizes highlights the importance of sufficient lidar
beam penetration to accurately characterize understory conditions
through the depth of the canopy. In addition to increasing the number
of lower canopy returns increasing the window size also accounts for
the neighboring canopy structure which impacts the local light environment. For our dataset a window size of 20 m enabled measurement of enough discrete lidar returns to accurately represent 3D variation in canopy structure as it controls vertical distribution in LMA. We
found increasing window beyond 20 m provided no benefit to modeling
within-canopy LMA because of decreasing spatial autocorrelation in

canopy structure, thus providing less horizontal detail in the vertical structure of canopies. For data collected under different sensor configurations this may differ as the ability of a lidar sensor adequately characterize canopy structure is not only a function of characteristics of the canopy itself, but also the lidar sensor properties, including beam power, wavelength, divergence and return density (Lim et al., 2003; Morsdorf et al., 2009; Jakubowski et al., 2013).

Other methods exist for estimating transmittance from discrete return lidar, but usually require a priori knowledge of species composition and age classes to define light extinction coefficients (Parker et al., 2002). We developed our method explicitly to operate independent of species composition information, which potentially makes it more flexible for application in new study areas lacking such information. Full waveform lidar offers the potential to provide greater detail on structural characteristics of forest canopies driving within-canopy radiation regimes compared to discrete return lidar, but was not used in this study due to a sensor malfunction. Waveform processing methods such as deconvolution and decomposition offer the ability to extract a greater number of returns (Zhou et al., 2017) or estimate backscattering cross sections (Wagner et al., 2006), that may relate more specifically to leaf/plant area.

Our modeling results highlight the importance of an accurate estimate of top-of-canopy LMA to characterize within-canopy vertical variation in LMA. We found that restricting the wavelength region to the far SWIR (2000–2450 nm) resulted in the best performing model, this region of the spectrum is known to contain absorption features related to dry matter content including proteins, starch, sugars and cellulose (Curran, 1989; Jacquemoud et al., 1996). Conversely models built using the full VNIR-SWIR range performed poorly, possibly a

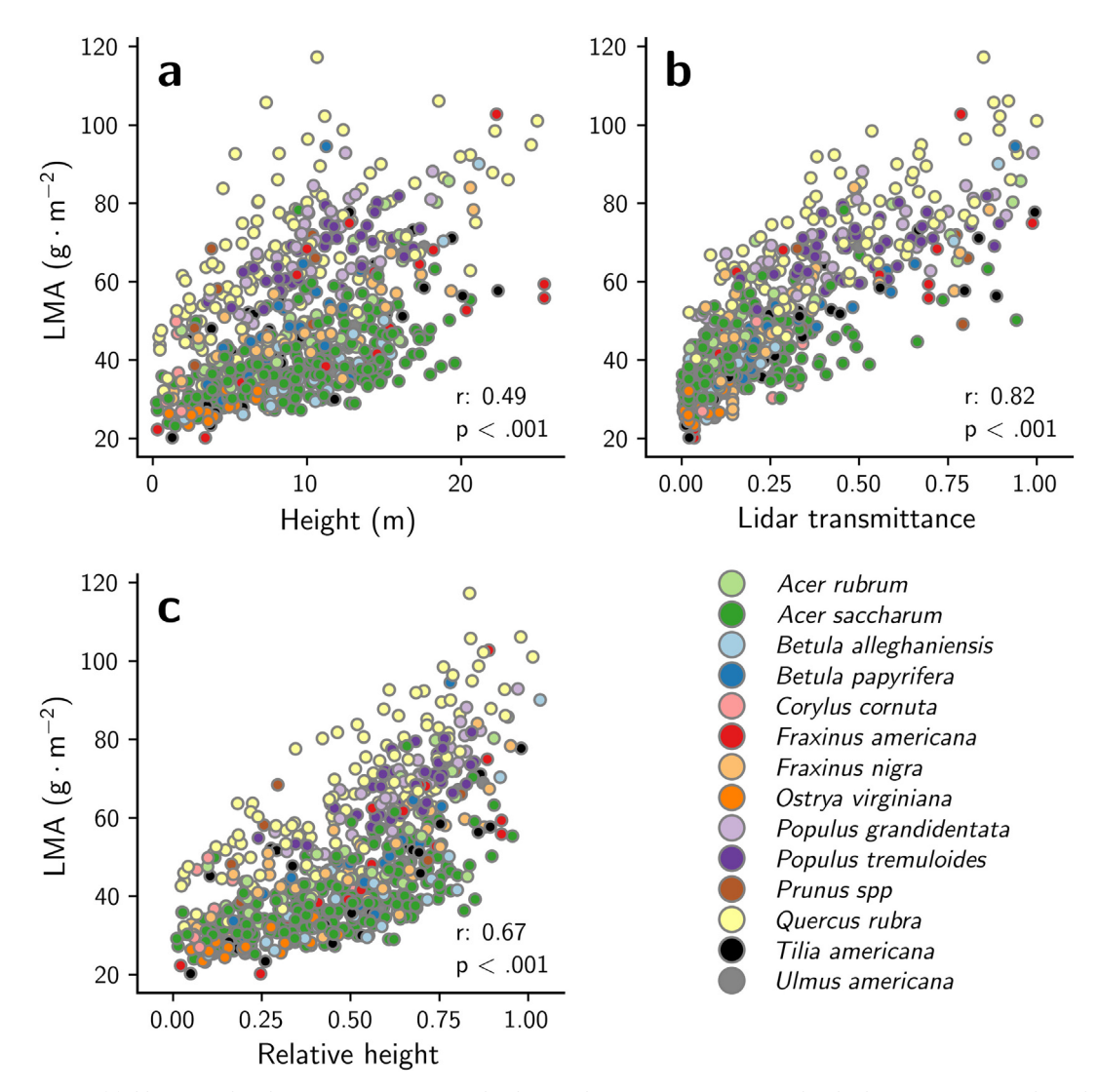


Fig. 6. Comparison of field-measured within-canopy LMA against the three within-canopy covariates: a) height, b) transmittance and c) relative height.

result of overfitting to pigment absorption features or canopy structure induced effects that are not generalizable across the entire dataset. Inclusion of top-of-canopy LMA as a predictor improved within-canopy model performance compared to models using only height and transmittance metrics as predictors (R²: 0.69 vs. 0.78; Supplemental Table S1). The top-of-canopy LMA serves two roles in the 3D model: first, it acts as a starting point for the within-canopy gradient of decreasing LMA and, second, it defines the slope of the relationship between LMA and transmittance, as plots with higher top-of-canopy LMA show steeper LMA declines within the canopy-i.e., larger values for the $\tau_{inv20m}(h) \cdot (\beta_0 + LMA_{toc} \cdot \beta_1 + rh_{inv}(h) \cdot \beta_2)$ term in Eq. (1) (see β coefficients in Table 3). The interaction terms in Eq. (2) modify the transmittance slope to account for the fact that LMA largely converges to a small range of values at the bottom of the canopy ($\sim 20-40 \text{ g m}^{-2}$) irrespective of the value at the top of the canopy, where the range of LMA is large (\sim 50-120 g m⁻²). Interestingly, our results suggest a generalized relationship describing within-canopy decreases in LMA in these temperate broadleaf deciduous forests, independent of either canopy species or subcanopy species identity (Fig. 6b and c). Our field data demonstrate that in multi-species plots, where species vary through the vertical profile, trends in LMA generally follow a continuous pattern regardless of species turnover (illustrated for individual plots in Fig. S6). Moreover not only do we see LMA decline within a given tree of a species, there is also vertical species-turnover that corresponds to shade tolerance, and these shade tolerant species also have lower LMA as well. The fact that these patterns can be modeled using remote sensing may enable testing the generality of the relationship across a range of broadleaf forest types.

Our model used relative rather than absolute height above ground as an independent variable, and moreover we show that absolute height had a weaker explanatory power than relative height (Supplemental Table S1). While others have shown a strong relationship between LMA and absolute height (Koch et al., 2004; Cavaleri et al., 2010), these studies have focused on much taller trees than in our study area. We expect that hydraulic constraints may play a weaker role in regulating LMA through the canopy in these northern temperate forests, and expect that a similar model may need to leverage absolute height for taller forests in which absolute height plays a more significant hydraulic role on leaf development. It is not clear what physiological process relative height captures in our model, although it may simply be compensating for limitations in characterizing lower canopy vertical structure due to lidar beam attenuation or covarying with other environmental conditions driving LMA variation like temperature, humidity or windspeed.

Ultimately, the utility in our new approach will be the generation of voxels to represent 3D trait variation, potentially applicable for modeling canopy processes. However, our 2-dimensional maps of 3D patterns in LMA reveal unique patterns not visible from the visible imagery (Fig. 9a,c). In particular, the maps highlight the legacies of logging, selective logging and other disturbances. This results in highly variable, but spatially coherent patterns in within-canopy LMA that is otherwise

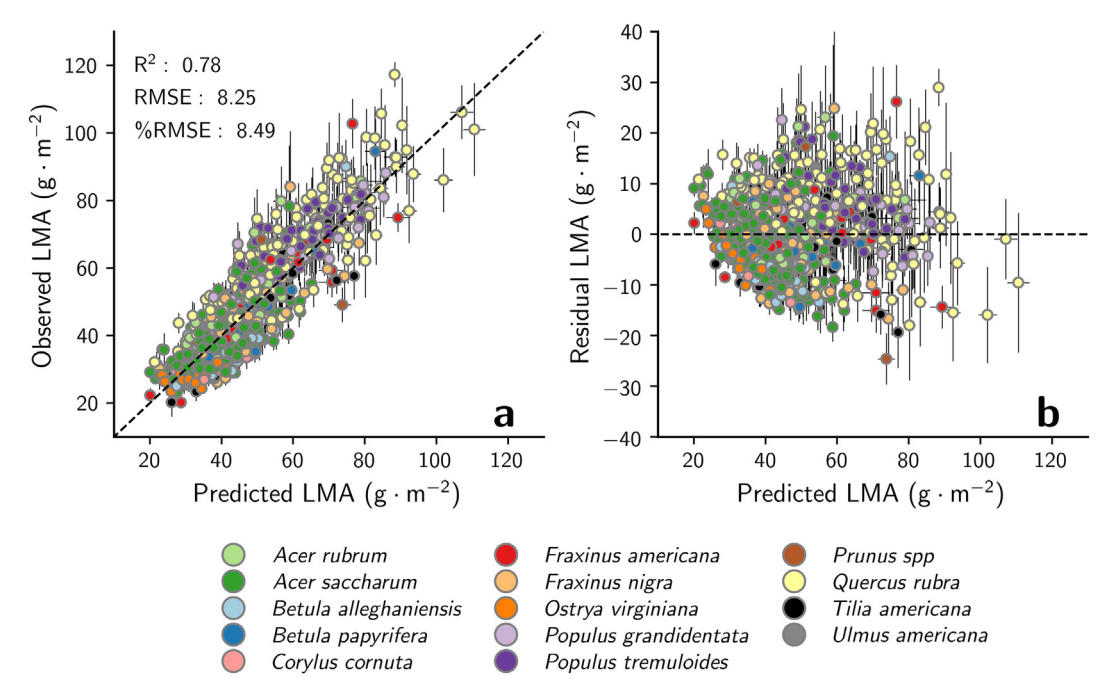


Fig. 7. Out-of-sample results for best-performing within-canopy LMA model. a) Predicted versus observed scatter plot; b) Residual plot; X-axis error bars indicate +/-1 standard deviation of out-of-sample LMA estimates across 5 cross-validation iterations; Y-axis error bars indicate +/-1 standard deviation of within-sample field measured LMA.

obscured by relatively dense stands. Of note are the variable patterns seen in the three oak stands highlighted in Fig. 9, a thinned oak stand (To), a closed canopy oak stand (Co) and an open-grown oak stand (Oo). At the top of the canopy the thinned and closed stands show similar values in LMA, 104 and 105 g m⁻², respectively, while the opengrown stand is much higher at 119 g m⁻². This difference may be a result of site-specific differences in local microclimate and/or soil moisture in the open-grown site relative to the closed and thinned sites, resulting in higher LMA (Potter et al., 2001; Abrams et al., 1994). However, when comparing within-canopy gradients in LMA the closed and thinned sites quickly diverge. The closed stand shows a sharp decline in LMA through the canopy while the within-canopy gradient of LMA in the thinned stand is shallower owing to increased light penetration, a pattern that is consistent with experimental treatments (Chiang and Brown, 2010). A key insight from this effort is not only that canopy structure is spatially heterogeneous and hence so is full-canopy LMA, but that this variation may be significant to our understanding of within-canopy processes. This also important for understanding patterns of forest function, as the majority of temperate forests in this region have undergone some level of stand management or disturbance that is not apparent in passive imaging.

While this study focused on within-canopy patterns of LMA, other physiologically and ecologically relevant foliar traits also vary along canopy environmental gradients, including concentrations of total non-structural carbohydrates (Niinemets, 1997) and phosphorus (Leuning et al., 1991), and chlorophyll to nitrogen ratios (Koike et al., 2001). Although not included in this study due to a lack of validation data, we also estimated a suite of traits using fresh-leaf and dry-ground spectroscopic models and found significant within-canopy patterns in several traits correlated with lidar transmittance including sugar concentration, chlorophyll A content and xanthophyll cycle pigment content (violaxanthin, antheraxanthin and zeaxanthin (VAZ)) (Supplemental Fig. S5). VAZ, which play a photoprotective role in leaves and are known to correlate positively with light levels/transmittance, showed the strongest relationship with transmittance among the traits estimated (R² = 0.49) (Niyogi et al., 1997; Hansen et al., 2002).

Here we focused on a single period of the growing season, but LMA is known to vary through the course of the growing season (Reich et al., 1991; Yang et al., 2016). In addition to seasonal variation in absolute values of LMA, there may also be phenological variations in the relationship between top-of-canopy LMA and within-canopy LMA as it relates to forest vertical structure. For example, Coble et al. (2016)

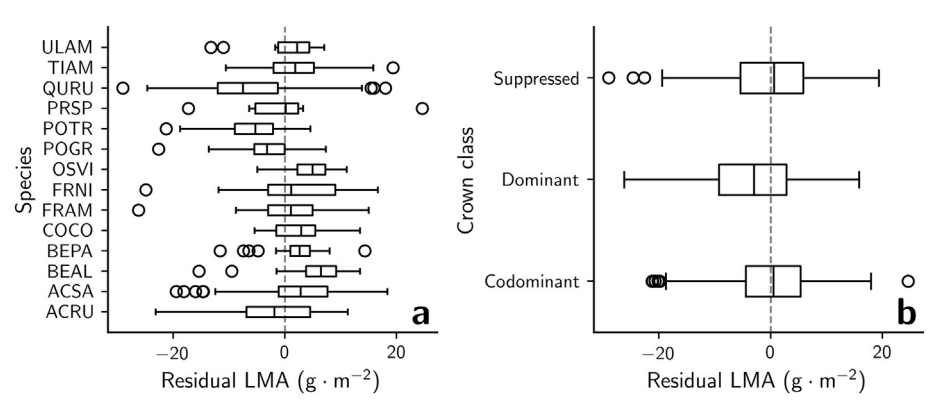


Fig. 8. Distribution of within-canopy residuals grouped by a) species and b) crown class.

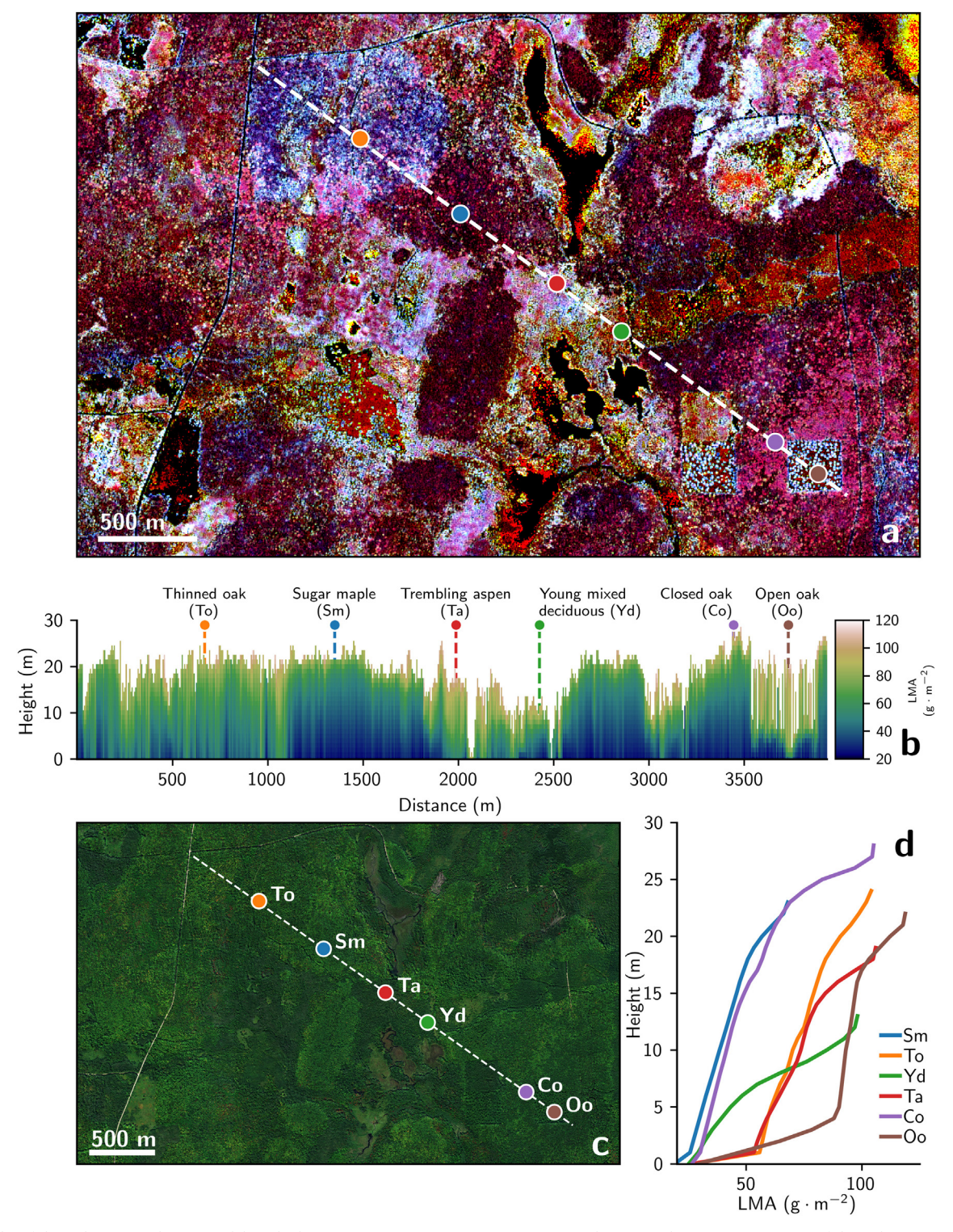


Fig. 9. Results of three-dimensional LMA model applied to CHEQ (90.069°W, 45.795° N). a) Two-dimensional RGB representation of three-dimensional patterns in LMA, R: Top-of-canopy LMA, G: LMA 5 m into canopy, B: LMA 10 m into canopy. b) Profile view of LMA transect; c) True color RGB image d) Height versus LMA for a set of individual 5 m pixels from forest types located on transect. Forest types: Thinned oak (To), Sugar maple (Sa), Trembling aspen (Ta), Young mixed deciduous (Yd), Closed canopy oak (Co), Open-grown oak (Oo).

found that drivers of within-canopy variability in LMA in sugar maples varied during the growing season, driven by height early in the growing season and light environment later in the growing season. This suggests future directions of research in both ecological and remote sensing research testing the extent to which the relationships we describe are generalizable throughout the course of the growing season. This may also necessitate further testing the extent to which species identity

conditions temporal patterns in 3D LMA.

As well, this study is specific to northern temperate broadleaf forests, and was not tested on similar species in other biomes, nor on physiognomically or physiologically different tree types such as conifers and evergreen broadleaves. We expect that different forest types will exhibit a generalizable pattern, a decrease in LMA with depth into the canopy, but due to differences in resource allocation strategies and

Table 3
Within-canopy mean permuted model coefficients.

Coefficient	Estimate
β_0	40.19
β_1	-0.80
β_2	-34.83

Table 4Within-canopy LMA cross-validation metrics by species.

Species	R^2	RMSE	NRMSE
Acer rubrum	0.69	8.13	0.15
Acer saccharum	0.5	7.02	0.13
Betula alleghaniensis	0.8	8.53	0.13
Betula papyrifera	0.86	5.62	0.09
Corylus cornuta	0.7	5.72	0.24
Fraxinus americana	0.78	9.37	0.11
Fraxinus nigra	0.63	8.37	0.14
Ostrya virginiana	0.35	6.08	0.47
Populus grandidentata	0.84	6.38	0.15
Populus tremuloides	0.5	8.6	0.3
Prunus spp.	0.51	9.71	0.27
Quercus rubra	0.77	11.14	0.13
Tilia americana	0.75	7.33	0.13
Ulmus americana	0.91	6.5	0.15

canopy structure, the shapes of the relationships will differ. Future testing of the generality of our model could apply the model to different forest types to identify how model coefficients change by taxa.

Our mapping of 3D patterns in LMA has the potential to be coupled with recent efforts to model vertical LAI profiles and leaf area density using lidar (Tang et al., 2012; Kamoske et al., 2019) as a basis to estimate full canopy foliar biomass and nutrient content for use as inputs into fire (Perry et al., 2004), nutrient cycling (Grimm et al., 2003) and carbon accounting models (Hudiburg et al., 2009). Extensive airborne and spaceborne lidar (e.g., GEDI) combined with imaging spectroscopy may enable better characterization of the distribution of within-canopy processes, even if wall-to-wall mapping is not yet possible. Multi-layer canopy photosynthesis models that incorporate expected variation in physiologically important traits throughout the canopy can provide more accurate estimates of assimilation rates than more generalized methods like big-leaf models (Raulier et al., 1999). However, at present, most models do not explicitly include 3D variation in foliar traits.

5. Conclusion

This study is the first to employ imaging spectroscopy and lidar together to map 3D patterns in LMA, an important canopy functional trait that is widely used to characterize photosynthetic capacity of forests. Our method accurately estimated horizontal and vertical variation in LMA in broadleaf forests without taking into account species composition ($R^2 = 0.82$; RMSE: 8.5 g m⁻²). Our work is an initial step, with further research into the generality of the relationships needed across different sensors, ecosystems and through time. As well, the integration of these data products into ecosystem process models requires testing. Critical to this research was the availability of coincident free and open high-resolution leaf-on lidar and imaging spectroscopy data, which until the NEON AOP was deployed was rare. Separately, each technology addresses different needs, but the true value of imaging spectroscopy and lidar may be in their combined, complementary use. Finally, new or planned spaceborne hyperspectral (ie. PRISMA, HISUI, CHIME and SBG) and lidar systems (GEDI) will provide opportunities to build on our work and quantify full-canopy physiological variation on a global scale.

Data availability

Field data, leaf-level spectra, and extracted remote sensing data can be found on the EcoSIS spectral repository (https://ecosis.org/). Leaf and canopy-level spectral models can be found on the Ecological Spectral Model Library site (https://ecosml.org/). AOP imaging spectroscopy and lidar data are available for download from NEON (https://data.neonscience.org/).

Declaration of Competing Interest

The authors declare the following financial interests/personal relationships which may be considered as potential competing interests.

Acknowledgments

We thank Andrew Jablonski, Aidan Mazur, Benjamin Spaier, John Clare, Brendan Heberlein, Ittai Herrmann, Abigail Ernst, Hannah Manninen and Alex Brito for providing field assistance. We are also grateful to Tedward Erker for providing valuable insights into the statistical analysis and Tristan Goulden for guidance on NEON data processing. This work was supported by NSF Macrosystems Biology and Early NEON Science Grant 1638720 and USDA McIntire-Stennis awards WIS1809 and WIS3008 to PAT and ELK.

Appendix A. Supplementary Data

Supplementary data to this article can be found online at https://doi.org/10.1016/j.rse.2020.112043.

References

- Abrams, M.D., Kubiske, M.E., Mostoller, S.A., 1994. Relating wet and dry year ecophysiology to leaf structure in contrasting temperate tree species. Ecology 75 (1), 123–133.
- Ali, A.M., Skidmore, A.K., Darvishzadeh, R., van Duren, I., Holzwarth, S., Mueller, J., 2016. Retrieval of forest leaf functional traits from HySpex imagery using radiative transfer models and continuous wavelet analysis. ISPRS J. Photogramm. Remote Sens. 122, 68–80
- Aranda, I., Pardo, F., Gil, L., Pardos, J.A., 2004. Anatomical basis of the change in leaf mass per area and nitrogen investment with relative irradiance within the canopy of eight temperate tree species. Acta Oecol. 25 (3), 187–195.
- Asner, G.P., Anderson, C.B., Martin, R.E., Tupayachi, R., Knapp, D.E., Sinca, F., 2015. Landscape biogeochemistry reflected in shifting distributions of chemical traits in the Amazon forest canopy. Nat. Geosci. 8 (7), 567–573.
- Bates, Douglas, Machler, Martin, Bolker, Ben, et al., 2015. Fitting Linear Mixed-Effects Models Using Ime4. Journal of Statistical Software 67 (1), 1–48. https://doi.org/10. 18637/jss.v067.i01.
- Cavaleri, M.A., Oberbauer, S.F., Clark, D.B., Clark, D.A., Ryan, M.G., 2010. Height is more important than light in determining leaf morphology in a tropical forest. Ecology 91 (6), 1730–1739.
- Chadwick, K., Asner, G., 2016. Organismic-scale remote sensing of canopy foliar traits in lowland tropical forests. Remote Sens. 8 (2), 87.
- Chiang, J.M., Brown, K.J., 2010. The effects of thinning and burning treatments on within-canopy variation of leaf traits in hardwood forests of Southern Ohio. For. Ecol. Manag. 260 (6), 1065–1075.
- Coble, A.P., Cavaleri, M.A., 2014. Light drives vertical gradients of leaf morphology in a sugar maple (Acer saccharum) forest. Tree Physiol. 34 (2), 146–158.
- Coble, A.P., VanderWall, B., Mau, A., Cavaleri, M.A., 2016. How vertical patterns in leaf traits shift seasonally and the implications for modeling canopy photosynthesis in a temperate deciduous forest. Tree Physiol. 36 (9), 1077–1091.
- Cohen, W.B., Goward, S.N., 2004. Landsat's role in ecological applications of remote sensing. Bioscience 54 (6), 535–545.
- Colgan, M., Baldeck, C., Féret, J.B., Asner, G., 2012. Mapping savanna tree species at ecosystem scales using support vector machine classification and BRDF correction on airborne hyperspectral and LiDAR data. Remote Sens. 4 (11), 3462–3480.
- Curran, P.J., 1989. Remote sensing of foliar chemistry. Remote Sens. Environ. 30 (3), 271–278.
- Dupuis, D.J., Hamilton, D.C., 2000. Regression residuals and test statistics: assessing naive outlier deletion. Can. J. Stat. 28 (2), 259–275.
- Ellsworth, D.S., Reich, P.B., 1993. Canopy structure and vertical patterns of photosynthesis and related leaf traits in a deciduous forest. Oecologia 96 (2), 169–178.
- Fleck, S., Van Der Zande, D., Schmidt, M., Coppin, P., 2004. Reconstructions of tree structure from laser-scans and their use to predict physiological properties and processes in canopies. Int. Arch. Photogramm. Remote. Sens. Spat. Inf. Sci. 36 (8), W2.

- Gelman, A., Hill, J., 2007. Data Analysis Using Regression and Hierarchical/Multilevel Models. Cambridge, New York, NY.
- Goulden, T., 2019. Neon Algorithm Theoretical Basis Document (ATBD): Neon Elevation (DTN and DSM). (Technical Report NEON.DOC.002390, NEON).
- Grimm, N.B., Gergel, S.E., McDowell, W.H., Boyer, E.W., Dent, C.L., Groffman, P., ... McClain, M.E., 2003. Merging aquatic and terrestrial perspectives of nutrient biogeochemistry. Oecologia 137 (4), 485–501.
- Hansen, U., Fiedler, B., Rank, B., 2002. Variation of pigment composition and anti-oxidative systems along the canopy light gradient in a mixed beech/oak forest: a comparative study on deciduous tree species differing in shade tolerance. Trees 16 (4-5), 354-364.
- Hudiburg, T., Law, B., Turner, D.P., Campbell, J., Donato, D., Duane, M., 2009. Carbon dynamics of Oregon and Northern California forests and potential land-based carbon storage. Ecol. Appl. 19 (1), 163–180.
- Jacquemoud, S., Ustin, S.L., Verdebout, J., Schmuck, G., Andreoli, G., Hosgood, B., 1996.
 Estimating leaf biochemistry using the PROSPECT leaf optical properties model.
 Remote Sens. Environ. 56 (3), 194–202.
- Jakubowski, M.K., Guo, Q., Kelly, M., 2013. Tradeoffs between lidar pulse density and forest measurement accuracy. Remote Sens. Environ. 130, 245–253.
- Kamoske, A.G., Dahlin, K.M., Stark, S.C., Serbin, S.P., 2019. Leaf area density from airborne LiDAR: comparing sensors and resolutions in a temperate broadleaf forest ecosystem. For. Ecol. Manag. 433, 364–375.
- Kampe, T., Gallery, W., Goulden, T., Leisso, K., Krause, K., 2016. NEON Imaging Spectrometer Geolocation Algorithm Theoretical Basis Document. (Technical Report NEON.DOC.001290, NEON).
- Kampe, T.U., Johnson, B.R., Kuester, M.A., Keller, M., 2010. NEON: the first continental-scale ecological observatory with airborne remote sensing of vegetation canopy biochemistry and structure. J. Appl. Remote. Sens. 4 (1), 043510.
- Kampe, T.U., McCorkel, J., Hamlin, L., Green, R.O., Krause, K.S., Johnson, B.R., 2011. Progress in the development of airborne remote sensing instrumentation for the National Ecological Observatory Network. In remote sensing and modeling of ecosystems for sustainability VIII. Int. Soc. Opt. Photonics 8156, 81560A.
- Koch, G.W., Sillett, S.C., Jennings, G.M., Davis, S.D., 2004. The limits to tree height. Nature 428 (6985), 851.
- Koike, T., Kitao, M., Maruyama, Y., Mori, S., Lei, T.T., 2001. Leaf morphology and photosynthetic adjustments among deciduous broad-leaved trees within the vertical canopy profile. Tree Physiol. 21 (12–13), 951–958.
- Le Maire, G., François, C., Soudani, K., Berveiller, D., Pontailler, J.Y., Bréda, N., ... Dufrêne, E., 2008. Calibration and validation of hyperspectral indices for the estimation of broadleaved forest leaf chlorophyll content, leaf mass per area, leaf area index and leaf canopy biomass. Remote Sensing of Environment. 112 (10), 3846–3864.
- Lefsky, M.A., Cohen, W.B., Parker, G.G., Harding, D.J., 2002. Lidar remote sensing for ecosystem studies: Lidar, an emerging remote sensing technology that directly measures the three-dimensional distribution of plant canopies, can accurately estimate vegetation structural attributes and should be of particular interest to forest, landscape, and global ecologists. BioScience 52 (1), 19–30.
- Leuning, R., Cromer, R.N., Rance, S., 1991. Spatial distributions of foliar nitrogen and phosphorus in crowns of *Eucalyptus grandis*. Oecologia. 88 (4), 504–510.
- Li, B., Morris, J., Martin, E.B., 2002. Model selection for partial least squares regression. Chemom. Intell. Lab. Syst. 64 (1), 79–89.
- Lim, K., Treitz, P., Wulder, M., St-Onge, B., Flood, M., 2003. LiDAR remote sensing of forest structure. Prog. Phys. Geogr. 27 (1), 88–106.
- Messier, J., McGill, B.J., Lechowicz, M.J., 2010. How do traits vary across ecological scales? A case for trait-based ecology. Ecol. Lett. 13 (7), 838–848.
- Messier, J., McGill, B.J., Enquist, B.J., Lechowicz, M.J., 2017. Trait variation and integration across scales: is the leaf economic spectrum present at local scales? Ecography 40 (6), 685–697.
- Morsdorf, F., Nichol, C., Malthus, T., Woodhouse, I.H., 2009. Assessing forest structural and physiological information content of multi-spectral LiDAR waveforms by radiative transfer modelling. Remote Sens. Environ. 113 (10), 2152–2163.
- Niinemets, \ddot{U} ., 1997. Role of foliar nitrogen in light harvesting and shade tolerance of four temperate deciduous woody species. Funct. Ecol. 11 (4), 518–531.
- Niinemets, Ü., 1999. Research review. Components of leaf dry mass per area-thickness and density-alter leaf photosynthetic capacity in reverse directions in woody plants. New Phytol. 144 (1), 35–47.
- Niinemets, \dot{U} , 2001. Global-scale climatic controls of leaf dry mass per area, density, and thickness in trees and shrubs. Ecology 82 (2), 453–469.
- Niinemets, Ü., Keenan, T.F., Hallik, L., 2015. A worldwide analysis of within-canopy variations in leaf structural, chemical and physiological traits across plant functional types. New Phytol. 205 (3), 973–993.
- Niyogi, K.K., Björkman, O., Grossman, A.R., 1997. The roles of specific xanthophylls in photoprotection. Proc. Natl. Acad. Sci. 94 (25), 14162–14167.
- Olpenda, A.S., Stereńczak, K., Będkowski, K., 2018. Modeling solar radiation in the forest using remote sensing data: a review of approaches and opportunities. Remote Sens. 10 (5), 694.
- Ourcival, J.M., Joffre, R., Rambal, S., 1999. Exploring the relationships between reflectance and anatomical and biochemical properties in Quercus ilex leaves. New Phytol. 143 (2), 351–364.
- Parker, G.G., Lefsky, M.A., Harding, D.J., 2001. Light transmittance in forest canopies determined using airborne laser altimetry and in-canopy quantum measurements. Remote Sens. Environ. 76 (3), 298–309.
- Parker, G.G., Davis, M.M., Chapotin, S.M., 2002. Canopy light transmittance in Douglas-

- fir-Western hemlock stands. Tree Physiol. 22 (2-3), 147-157.
- Pedregosa, Fabian, Varoquaux, Gaël, Gramfort, Alexandre, Michel, Vincent, Thirion, Bertrand, Grisel, Olivier, Blondel..., Mathieu, 2011. Scikit-learn: machine learning in Python. J. Mach. Learn. Res. 12, 2825–2830.
- Perry, D.A., Jing, H., Youngblood, A., Oetter, D.R., 2004. Forest structure and fire susceptibility in volcanic landscapes of the Eastern high cascades, Oregon. Conserv. Biol. 18 (4), 913–926.
- Peterson, D.L., Aber, J.D., Matson, P.A., Card, D.H., Swanberg, N., Wessman, C., Spanner, M., 1988. Remote sensing of forest canopy and leaf biochemical contents. Remote Sens. Environ. 24 (1), 85–108.
- Petter, G., Wagner, K., Wanek, W., Sánchez Delgado, E.J., Zotz, G., Cabral, J.S., Kreft, H., 2016. Functional leaf traits of vascular epiphytes: vertical trends within the forest, intra-and interspecific trait variability, and taxonomic signals. Funct. Ecol. 30 (2), 188–198.
- Poorter, H., Niinemets, Ü., Poorter, L., Wright, L.J., Villar, R., 2009. Causes and consequences of variation in leaf mass per area (LMA): a meta-analysis. New Phytol. 182 (3), 565–588.
- Potter, B.E., Teclaw, R.M., Zasada, J.C., 2001. The impact of forest structure on nearground temperatures during two years of contrasting temperature extremes. Agric. For. Meteorol. 106 (4), 331–336.
- Poulter, A.G., Olbrich, B.W., Dye, P.J., 1991. Sampling shoots from tall canopies with a balloon-hoisted cutting device. Aust. For. 54 (1–2), 109–110.
- Raulier, F., Bernier, P.Y., Ung, C.H., 1999. Canopy photosynthesis of sugar maple (Acer saccharum): comparing big-leaf and multilayer extrapolations of leaf-level measurements. Tree Physiol. 19 (7), 407–420.
- Reich, P.B., Walters, M.B., Ellsworth, D.S., 1991. Leaf age and season influence the relationships between leaf nitrogen, leaf mass per area and photosynthesis in maple and oak trees. Plant Cell Environ. 14 (3), 251–259.
- Richter, R., Schläpfer, D., 2015. Atmospheric/topographic correction for airborne imagery. ATCOR-4 user guide. (Version 7.0.0).
- Rogers, A., Medlyn, B.E., Dukes, J.S., Bonan, G., Von Caemmerer, S., Dietze, M.C., ...
 Prentice, I.C, 2017. A roadmap for improving the representation of photosynthesis in Earth system models. New Phytologist. 213 (1), 22–42.
- Roughgarden, J., Running, S.W., Matson, P.A., 1991. What does remote sensing do for ecology? Ecology 72 (6), 1918–1922.
- Schläpfer, D., Richter, R., Feingersh, T., 2014. Operational BRDF effects correction for wide-field-of-view optical scanners (BREFCOR). IEEE Trans. Geosci. Remote Sens. 53 (4), 1855–1864.
- Serbin, S.P., Singh, A., McNeil, B.E., Kingdon, C.C., Townsend, P.A., 2014. Spectroscopic determination of leaf morphological and biochemical traits for Northern temperate and boreal tree species. Ecol. Appl. 24 (7), 1651–1669.
- Serbin, S.P., Wu, J., Ely, K.S., Kruger, E.L., Townsend, P.A., Meng, R., ... Rogers, A., 2019. From the Arctic to the tropics: multi-biome prediction of leaf mass per area using leaf reflectance. New Phytologist. 224 (4), 1557–1568.
- Sigrist, P., Coppin, P., Hermy, M., 1999. Impact of forest canopy on quality and accuracy of GPS measurements. Int. J. Remote Sens. 20 (18), 3595–3610.
- Singh, A., Serbin, S.P., McNeil, D.E., Kingdon, C.C., Townsend, P.A., 2015. Imaging spectroscopy algorithms for mapping canopy foliar chemical and morphological traits and their uncertainties. Ecol. Appl. 25 (8), 2180–2197.
- Tang, H., Dubayah, R., Swatantran, A., Hofton, M., Sheldon, S., Clark, D.B., Blair, B., 2012. Retrieval of vertical LAI profiles over tropical rain forests using waveform lidar at La Selva, Costa Rica. Remote Sens. Environ. 124, 242–250.
- Todd, K.W., Csillag, F., Atkinson, P.M., 2003. Three-dimensional mapping of light transmittance and foliage distribution using lidar. Can. J. Remote. Sens. 29 (5), 544–555.
- Vose, J.M., Clinton, B.D., Sullivan, N.H., Bolstad, P.V., 1995. Vertical leaf area distribution, light transmittance, and application of the beer–Lambert law in four mature hardwood stands in the southern Appalachians. Can. J. For. Res. 25 (6), 1036–1043.
- Wagner, W., Ullrich, A., Ducic, V., Melzer, T., Studnicka, N., 2006. Gaussian decomposition and calibration of a novel small-footprint full-waveform digitising airborne laser scanner. ISPRS J. Photogramm. Remote Sens. 60 (2), 100–112.
- Wang, Z., Townsend, P.A., Schweiger, A.K., Couture, J.J., Singh, A., Hobbie, S.E., Cavender-Bares, J., 2019. Mapping foliar functional traits and their uncertainties across three years in a grassland experiment. Remote Sens. Environ. 221, 405–416.
- Wang, Z., Chlus, A., Geygan, R., Ye, Z., Zheng, T., Singh, A., Couture, J.J., Cavender-Bares, J., Kruger, E.L., Townsend, P.A., 2020. Foliar functional traits from imaging spectroscopy across biomes in Eastern North America. New Phytol.
- Wold, S., Sjöström, M., Eriksson, L., 2001. PLS-regression: a basic tool of chemometrics. Chemom. Intell. Lab. Syst. 58 (2), 109–130.
- Wright, I.J., Reich, P.B., Westoby, M., Ackerly, D.D., Baruch, Z., Bongers, F., ... Flexas, J., 2004. The worldwide leaf economics spectrum. Nature 428 (6985), 821.
- Wu, T., Zhang, P., Zhang, L., Wang, G.G., Yu, M., 2016. Morphological response of eight Quercus species to simulated wind load. PLoS One 11 (9).
- Yang, X., Tang, J., Mustard, J.F., Wu, J., Zhao, K., Serbin, S., Lee, J.E., 2016. Seasonal variability of multiple leaf traits captured by leaf spectroscopy at two temperate deciduous forests. Remote Sens. Environ. 179, 1–12.
- Zhao, K., Valle, D., Popescu, S., Zhang, X., Mallick, B., 2013. Hyperspectral remote sensing of plant biochemistry using Bayesian model averaging with variable and band selection. Remote Sens. Environ. 132, 102–119.
- Zhou, T., Popescu, S.C., Krause, K., Sheridan, R.D., Putman, E., 2017. Gold-a novel deconvolution algorithm with optimization for waveform LiDAR processing. ISPRS J. Photogramm. Remote Sens. 129, 131–150.